Automatic and time-resolved determination of fracture characteristics from *in situ* experiments

K. Schmuck [a,*], M. Antenreiter [b], M. Alfreider [a], D. Kiener [a]

[a] *Montanuniversität Leoben, Department of Materials Science, Chair of Materials Physics, Jahnstraße 12, Leoben, 8700, Austria*
[b] *Montanuniversität Leoben, Department Mathematics and Information Technology, Chair of Information Technology, Erzherzog-Johann-Straße 3, Leoben, 8700, Austria*

ARTICLE INFO

ABSTRACT

The characterization of materials in ever smaller dimensions is crucial for the growing demand for miniaturized devices. Hence, *in situ* fracture experiments are frequently performed at the micron to sub-micron scale. To evaluate fracture process of these experiments, knowledge of the crack length or the crack tip opening displacement is required. Acquired *in situ* frames provide a direct measurement of the crack length, crack tip opening displacement and -angle. An algorithm was developed to extract these parameters from the *in situ* frame sequences automatically. To verify the performance of the algorithm, fracture characteristics were measured manually for several frames of the available *in situ* experiments. The fracture behavior of these samples ranged from brittle over semi-brittle to ductile. The comparison between algorithmic results and manual measurements demonstrated the applicability of the algorithm to different fracture behaviors. Additionally, the fracture characteristics determined by the algorithm are in accordance with the fracture toughness data reported in literature. The crack tip opening displacement measurement gives thorough insight into the plastic deformation during fracture. The automatic extraction of the fracture characteristics allows a more detailed analysis of small-scale fracture processes and enables a reproducible, continuous evaluation of the fracture characteristics of all frames.

1. Introduction

The ongoing trend of device miniaturization and decreasing internal length scales requires testing of material properties, including fracture behavior, on increasingly smaller length scales, down to the micron and sub-micron regime [1,2]. To gain insights into the material- and fracture behavior at this scale, *in situ* experiments are frequently conducted [1,3–5]. In these experiments, the plastic zone ahead of the crack tip extends over a considerable part of the ligament, which makes the application of elastic-plastic fracture mechanics (EPFM) necessary. The fracture evaluation in the framework of EPFM requires an accurate knowledge of the crack length. At the micron to sub-micron scale, crack length can be indirectly determined by measuring sample stiffness, which gives an average crack length over the crack front. Alternatively, crack length can be measured directly from acquired *in situ* frames [6–10]. Manual crack length measurement on all acquired frames is a tedious task and strongly depending on human individuality. Schmuck et al. [11] introduced an algorithm to extract the crack length from all frames semi-automatically by using image processing techniques. Their algorithm necessitates fine tuning of the evaluation parameters by the user.

Another characteristic parameter of fracture processes is the crack tip opening displacement (δ), which is a measure for crack tip blunting during the fracture process and is related to other fracture parameters through simplified models [8,12]. At the macro scale, it is possible to measure δ directly from a crack negative formed by filling the crack with a curing liquid, or indirectly via the hinge model, which relates the crack mouth opening displacement to δ via similar triangles [8,9,13–15]. The former is not applicable at the micron to sub-micron scale due to the small sample dimensions, though the hinge model is still applicable [8]. In addition, δ can be measured directly from *in situ* frames, which is frequently performed manually [16,17]. Manual measurements are a tedious and challenging task due to low resolution at the crack tip and image noise due to the high image acquisition rates necessary to capture crack growth. Often, as a result, only critical frames are evaluated manually.
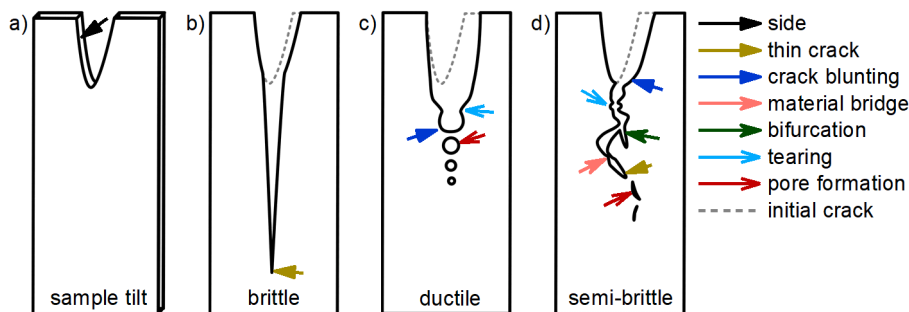
Fig. 1. Schematic illustration of the challenges to detect the crack contour and extract thereof the fracture characteristics from *in situ* images. a) Slightly tilted sample, viewing material from the back in the crack wake. b)-d) Different fracture types with the corresponding prominent fracture features. To access the colored version of this graphic the reader is referred to the online version of the article.

In this work, the algorithm proposed by Schmuck et al. [11] is further enhanced to work automatically and extended to extract δ and crack tip opening angle (α) in addition to the crack length. These additional characteristics offer further insight into the ongoing fracture process and enhance data interpretation. To demonstrate the algorithms capabilities, it is applied to samples of different length scales, from micron to sub-micron scale, and varying fracture behavior ranging from brittle to ductile, substantiating the applicability of the algorithm to a wide range of problems.

2. Materials and methods

The image-based evaluation of *in situ* fracture experiments faces various challenges, schematically illustrated in Fig. 1. Mounting the sample is one of them, as a few degree tilt leads to a distorted view and visible side surfaces of the sample, depicted by Fig. 1 a). Generally, the distortion is negligible due to low tilt angles. A few degrees tilt, however, are sufficient to image side surfaces, leading to visible edges from the backside and possible material within the crack wake. Furthermore, the fracture process itself contributes to the challenges of image-based evaluation. Brittle fracture exhibits minor crack tip blunting before abruptly failing between two *in situ* images. Although the crack path is usually straight, the resulting thin crack is only a faint feature on the *in situ* images, shown in Fig. 1 b). In case of ductile fracture, the crack exhibits extensive blunting, pore formation and tearing of the material between crack tip and pores, illustrated in Fig. 1 c). The pores enlarge until they are in contact with the crack tip, resulting into crack propagation. This is again followed by crack tip blunting, more pore formation and tearing of the material, depicted by the increasing size of the pores closer to the crack tip in Fig. 1 c). Semi-brittle failure combines the features occurring in brittle and ductile fracture and adds further fracture features, see Fig. 1 d). Thereby, the crack at the crack tip is rather thin. Additionally, the tearing leads to material bridges during crack propagation, which, upon cracking, leaves behind material in the crack wake. During the propagation the crack might also deflect and bifurcate, displayed in Fig. 1 d).

To summarize, thin crack paths resemble to be faint features on the *in situ* frame and crack deflection blurs the transition between blunting and crack flanks. Additionally, pore formation renders the crack tip position ambiguous due to residual material from tearing and bridging, while bifurcation causes an ill-defined crack tip due to multiple crack branches as reported in literature [18–20]. However, the transition between the different fracture types is smooth, hence, the features may combine or might be missing for individual experiments. All of these features complicate the extraction of the fracture characteristics.

2.1. Material

The algorithm was developed using *in situ* frames of tested single-edged notched cantilever bending beams. Fig. 2 illustrates the standard
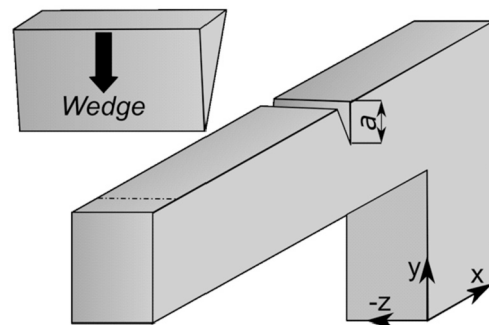

Fig. 2. Micro cantilever bending beam geometry, with a the crack length and a coordinate system. The z-direction refers to the viewing direction during the experiment, while the x- and y-direction span the image area.

geometry of these cantilevers. The fracture experiments were conducted in other publications and the cantilevers were fabricated from different materials, such as single crystalline tungsten, nano crystalline tungsten-copper composites and fully lamellar intermetallic titanium-alumina alloys [10,17,21]. Thereby, the cantilever size was situated in the micrometer regime. The cross-section of the cantilevers were approximately (3 x 3) μm^2 [10], (2.5 x 2.5) μm^2 [21], and from (5 x 5) μm^2 to (35 x 35) μm^2 [17]. To fabricate these cantilevers focused ion beam milling was employed. All fracture experiments were performed inside scanning electron microscopes (SEM; DSM 982, Carl Zeiss AG, Oberkochen, Germany; SEM/FIB, Leo 1540 XB, Carl Zeiss AG, Oberkochen, Germany). The *in situ* frames were acquired with the in-lens secondary electron detector at frame rates of either one [17], two [10] or six [21] frames per second. These frame rates provide a balance between image quality and ability to capture crack growth. Lower image acquisition rates benefit image quality, while higher are advantageous to capture crack growth. For cantilevers tested in [10,17], the imaging area was limited to the crack vicinity to enhance image quality and resolution. All cantilevers tested in [17] were loaded displacement controlled by quasi-static loading at rate of 50 nm/s with an ASMEC indenter (UNAT SEM 1, ASMEC GmbH, Dresden, Germany), which has a noise level of 50 µN in vaccum. This loading involved 15 partial unloading steps, enabling stiffness measurements to be determined during post-processing from the load-displacement data at each unloading step [8]. The cantilevers tested in [10,21] were tested in a force controlled scheme with a loading rate of 10 µN/s using a Hysitron Picoindenter PI 85 with a CSM module (Bruker Corporation, Billerica, USA). This indenter allows to perform dynamic loading and has a noise level of 1 µN. Thereby, the load signal is superimposed with a small sinusoidal signal, allowing the stiffness to be measured continuously [6]. The knowledge of stiffness in combination with the initial crack length allows the current crack length to be estimate from the mechanical data recorded [8,10]. This, mechanical data includes the load and displacement signal, as well as the stiffness signal in dynamical testing. The tips used
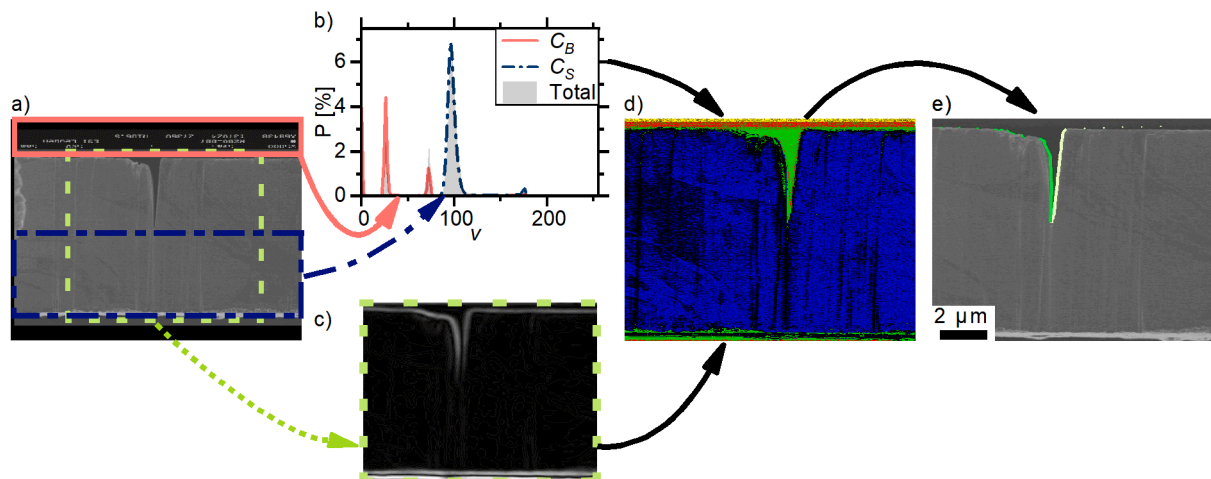
Fig. 3. Segmentation and contour extraction process. a) Defining background (red rectangle), sample (blue rectangle) and a region of interest around the crack (green rectangle). b) Histogram of the region of interest with the probability curves of sample (C_s) and background (C_b). c) Illustrates the edge probabilities found by the Sobel operator. d) Depicts the probabilities of sample (blue, channel), background (red, channel) and $f(x, y)$ (green, channel), as RGB-image. e) Extracted crack contour from the probability image. There the contour is partitioned into a left (dark green) and right (light green) part, respectively. To access the colored version of this graphic the reader is referred to the online version of the article.

for loading were in all cases wedge shaped conductive diamonds (Synton MDP, Nidau, Switzerland). For further information to the respective experimental procedure applied the reader is referred to the respective publications [10,17,21]. The investigated cantilevers exhibited a fracture behavior ranging from brittle to semi-brittle failure to cover the variety of crack features described above.

To further verify generalization, the algorithm was tested with *in situ* frames recorded by a transmission electron microscope (TEM, JEOL JEM-2200FS microscope, JEOL Ltd., Japan). The tested cantilever was fabricated from a titanium-aluminum alloy by focused ion beam milling and had a cross-section of about (200 x 150) nm^2. *In situ* frames were acquired in bright field mode at 1 frame per second. The sample exhibited additional distinct contrast changes over time due to dislocation movement. The cantilever was loaded displacement controlled by static loading with the Hysitron Picoindenter PI 85 and failed by extensive crack tip blunting.

2.2. Algorithm

The algorithm was written in Python 3.9 [22] using the image processing packages opencv (opencv-contrib-python-headless v4.6.0.66) [23] and sci-kit image (v0.19.2) [24] as well as the standard scientific packages numpy (v1.22.3) [25] and scipy (v1.8.0) [26]. To extract the fracture characteristics, the algorithm is split into preprocessing, pixel classification, crack flank contour retrieving and finally determination of the fracture characteristics from the extracted crack flanks, as detailed in the next chapters.

2.2.1. Image preprocessing

Depending on the experimental conditions, preprocessing is occasionally necessary. The algorithm assumes the following conditions: a top-down crack growth direction, consistent captured regions, and a consistent magnification across all frames. In cases of crack growth from bottom to top, the initial preprocessing involves a 180-degree rotation of all frames. Furthermore, the images sequences are split to include only images with a consistent magnification and region in case of different viewing areas or magnification during the experiment.

At small scale, thermal drift can significantly impact the result of the algorithm. Removing this drift from the frames is crucial to establish a consistently stable reference point across all frames. Determining accurate fracture characteristics, like crack length, requires a stable reference point. The algorithm achieves this by aligning each frame with

the previous frame using a registration technique known as phase cross-correlation [27], which provides the translative offset between two consecutive frames. To effectively align the frames, a region of interest (ROI) is selected to encompass the crack, ensuring that the crack remains within the ROI across all processed frames.

The algorithm is also sensitive to gray level changes between frames. Various recording devices might produce frames that are either darker or brighter by a constant factor. Shadowing or charging during the experiment can cause a change in gray scale distribution. Therefore, the algorithm compensates for constant gray level shifts between frames. In every frame, the median gray value in the ROI is calculated. The difference between two gray value medians is used to compensate for the variations in the recording process.

2.2.2. Pixel classification

After preprocessing, the objective is to classify each pixel in the image into two distinct classes. The first class, C_s, represents sample pixels, while the second class, C_b, denotes background pixels. The classification process relies on using the gray values of the pixels as a feature. To achieve this, the algorithm assigns each gray value v at position (x, y) within the range of $0 - 255$ to either the sample or background class based on a pre-calculated probability. The probability is determined by extracting gray values from user-defined regions in a reference frame. For the samples investigated, the initial frame was used as reference frame, as depicted in Fig. 3 a). Here, the red rectangle defines the gray values for the corresponding background pixels, while the blue rectangle represents gray values for sample pixels. By employing these rectangles, a probability function for each gray value is derived, indicating whether it belongs to the sample or background class. To avoid mathematical issues arising from probabilities with a zero value, a consistent small probability for each gray value and class is added. This small value is determined automatically by dividing one with the pixel count of the selected regions. The resulting probability distribution is illustrated in Fig. 3 b). The calculation of probabilities avoids a system with fixed absolute thresholds, because gray values can vary in each experiment, due to for example, differences in the interaction between the electron beam and sample, or the orientation of the scanned surface to the electron detector.

The gray values of the pixels are not always sufficient to assign a pixel to a class. Therefore, the algorithm incorporates edge information from crack contours by utilizing the Sobel operator [28] to extract additional information if a pixel belongs to an edge. This operator is de-

signed to highlight rapid changes in the image intensity. Rapid changes can be edges or noise from the image recording process. Therefore, usually a careful selected threshold has to be used at the end of an edge detection process. To avoid again the use of a fixed threshold, an automatic threshold adaption is implemented, described below in more detail.

The Sobel operator works by conducting a convolution of the image with a 3×3 kernel. The kernel emphasizes horizontal and vertical gradients in the image, enabling the identification of edges in both directions. The Sobel operator yields a low value if a pixel does not belong to an edge, but a high value if there are rapid changes in intensity, indicating a potential edge pixel. The Sobel operator, denoted as $S(x, y)$, does not provide probabilities. Therefore, the Sobel operator output cannot be combined with the probabilities from the gray values. To address this, the algorithm calculates S_{norm}, which falls within the range of 0.0 to 1.0, by normalizing it with the highest possible value of the Sobel operator.

After that, the values from grayscale and the edge information are combined by:

$$f(x, y) = 1 - P(v_{xy}|C_s) \cdot \left(1 - S_{\mathrm{norm}}(x, y)\right), \tag{1}$$

where v_{xy} is the gray value at position (x, y), $P(v_{xy}|C_s)$ is the likelihood that the gray value belongs to a sample pixel, and $S_{\mathrm{norm}}(x, y)$ is a kind of likelihood that the pixel at (x, y) is an edge pixel. The range of $f(x, y)$ is between 0.0 and 1.0 and can be interpreted as follows: high values correspond to pixels from background or strongly visible edges and low values of $f(x, y)$ indicate the pixel is likely part of the sample. Fig. 3 d) illustrates the combination of the class probabilities with $f(x, y)$, as RGB image. Thereby, the color channels correspond to the individual classes. The color value represents the probability that is assigned by the algorithm to that pixel for the respective class. In the case of black pixels the algorithm is uncertain and assigns the basis probability described above, which is approximately 0.

To distinguish between background and sample, a threshold is automatically chosen for the function $f(x, y)$ from the probabilities of the two classes. Pixels are assigned to class C_s based on the condition $P(v_{xy}|C_s) > P(v_{xy}|C_b)$ and the corresponding $f(x, y)$ values are calculated from these pixels by employing the 95th percentile $p^{0.95}_{sample}$. The second value of the threshold is calculated from the 5th percentile $p^{0.05}_{background}$ of all $f(x, y)$ with the condition $P(v_{xy}|C_s) < P(v_{xy}|C_b)$. By utilizing these two values, the threshold th is determined, which distinguishes between sample and the background.

$$th = \frac{p^{0.95}_{sample} + p^{0.05}_{background}}{2} \tag{2}$$

This automatic threshold adjustment is calculated for each frame to achieve the best possible separation between background and sample pixels.

2.2.3. Contour extraction

All background pixels that satisfy the condition $f(x, y) > th$ are connected from the above analysis with a fill algorithm. This operation can be described as pouring a liquid into the crack. For this a modified flood fill algorithm was employed [29,30]. The algorithm searches along a line for points that belong to the background. To fill the crack, the algorithm iterates over these points and analyzes the neighboring pixels. If the neighboring pixel belongs to the background, it is added to the list of points. The iteration stops if no further points are found. The resulting points list represents the filled form. Contours can be computed from this filled form. The lowest point of the fill operation separates the crack into a left and right contour (see Fig. 3 e).

The algorithm searches for crack-segments inside the sample by retrieving the outer sample contour and tests if regions with sufficient probability to be an edge are inside this contour. Crack segments are then connected by a shortest path search, which was proposed by Fred-

man et al. [31] and is implemented in the sci-kit image package [24]. The resulting path is a continuous pixel-thin path between the crack segments. This path is then split into sections that connect the respective crack segments. Starting from the lowest crack segment, each segment is convoluted with the path section that connects the current crack segment with the segment above. For the convolution the segments and sections are extracted into binary images, upon which the convolution is performed by discrete Fourier transformation of the binary images, multiplication in Fourier space and back transformation of the multiplication result. These are then added to the image with the filled crack to obtain the whole filled path, leading to a more natural crack shape. Segments with less than 4 px are neglected and assumed to be noise. This procedure allows the algorithm to overcome material bridges and barriers in the crack wake, which frequently occurs due to a possible sample tilt as well as generally during semi-brittle and ductile failure, as schematically illustrated in Fig. 1 a), c) and d).

2.2.4. Fracture characteristics

Determination of the crack tip opening displacement δ and -angle α is adopted from the description given by Shih [12]. The procedure is schematically shown for a representative blunted crack in Fig. 4 a) and b). The found contour lines are illustrated in Fig. 4 a), while b) depicts a closer view of the crack and measurement procedure. Fig. 4 c) shows the measurement for an ideally smooth crack. The angle α is measured by fitting both crack flanks linearly and measuring the angle between them, see the blue dotted lines in Fig. 4. The δ determination requires additional steps, involving defining the center line between the two fitted lines and constructing a symmetric right-angled triangle at the crack tip, which is projected on the center line, depicted in Fig. 4. In case of parallel lines, locating the center line is straightforward as it lies between the two fitted lines and is parallel to them. While otherwise two possibilities exist that are orthogonal. The line with the smaller orthogonal distance to the overall crack contour is used as center line, illustrated by the dashed violet line in Fig. 4. Next, the crack tip is projected onto this center line, which acts as intersection point and rotation center for two lines that are rotated by $\pm\frac{\pi}{4}$, see orange lines in Fig. 4. The intersection between these lines and the fitted crack flanks gives δ.

In general, the crack flanks are rather jagged, as illustrated by the representative crack in Fig. 4. The crack contour shows a variety of different shapes depending on the material behavior, ranging from brittle to ductile fracture [12,14,18,20,32]. To only fit the crack flanks and avoid the possible blunt region, the algorithm selects the fitting region by calculating the sliding variance with a 1D-kernel of size 11. This operation is applied to the x- and y-direction. By following the contour line, starting from the crack tip, the fit region begins where the y-variance is larger than the x-variance, as the blunted region would have an increased spread in x-direction. This requires a pronounced blunting region, which is only present in ductile and semi-brittle samples. Besides these measures the RANSAC algorithm [33,34] is employed to fit the crack flanks, since the algorithm is able to detect outliers and therefore neglects small blunting regions and portions of the jagged crack contour.

2.3. Fracture mechanics

To characterize fracture processes in EPFM the J-integral is used. The stress and strain fields in front of the crack tip can be modeled by the Hutchinson-Rice-Rosengren (HRR) theory [35,36]. As long as the fracture process is dominated by the HRR field [35,36], the fracture parameters δ and J are related according to:

$$\delta = d_n \frac{J_\delta}{\sigma_y}, \tag{3}$$

with σ_y as yield strength and d_n the Shih factor, which is 0.78 for a non-hardening material and plane strain-dominated fracture [12]. To
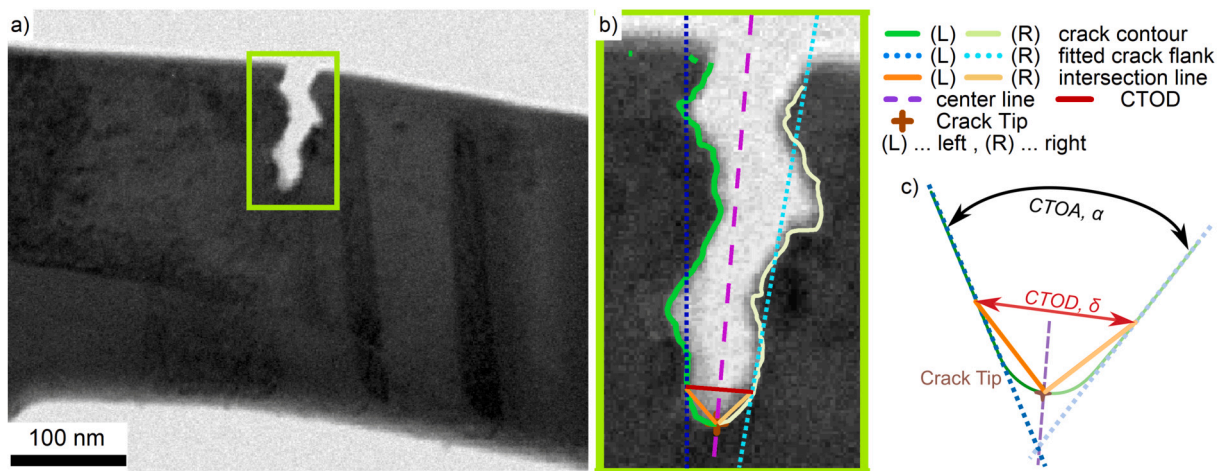
Fig. 4. Extraction process of crack tip opening displacement (δ) and -angle (α). a) Representative *in situ* frame with a blunted crack. b) Illustration of the crack region. c) illustration of the extraction for an ideal smooth crack. To access a colored version of this graphic the reader is referred to the online version of the article.

Table 1
Material properties at room temperature for the used materials with the yield strength (σ_y), the Young's modulus (E) and the Poisson ratio (ν).

Material	σ_y [MPa]	E [GPa]	ν
tungsten-copper (nc) [17]	2250	221	0.32
tungsten (sx) [10]	1750	410	0.28
titanium-aluminum [21,37]	660	189	0.23

compare the values with literature they can be converted into stress intensity values, given the plane strain assumptions, by [9]:

$$K = \sqrt{\frac{EJ}{1-\nu^2}}, \qquad (4)$$

with the Poisson ratio ν and the Young's modulus E. The material properties used in this work are tabulated in Table 1.

3. Results

3.1. Fracture behavior challenges

Results of the algorithm, crack tip coordinates, δ and α, were directly compared to manual measurements, which were performed for each *in situ* experiment on an evenly distributed subset of the acquired frames. The manual measurement was performed at least 3 times to allow for an uncertainty estimate. The crack tip coordinates were converted into crack extension (Δa) by calculating the Euclidean distance between the initial crack tip coordinates and all subsequent crack tip coordinates. This provides a comparison to the Δa approximated by the mechanical data in literature, where available. All values determined by the algorithm were smoothed by low-pass filtering. For reference, the unsmoothed data was plotted into the corresponding graphs in a light green color.

For the tested cantilevers, the fracture behavior was either brittle, semi-brittle or ductile. The brittle cantilevers fractured unstable, with a straight crack flank and only faint initial crack growth. Fig. 5 illustrates a brittle fracture cantilever, which was tested in [17]. Fig. 5 c) depicts Δa over time, including data obtained from mechanical evaluation, d) shows δ and e) α determined by the algorithm and manually. The unstable fracture occurred between two consecutive frames, resulting into a narrow crack, depicted by the fractured *in situ* frame in Fig. 5 b). Additionally, the processed frame is placed next to the acquired frame to illustrate the crack flanks found by the algorithm, highlighted by the green lines in Fig. 5 a) and b). The dark and bright green lines represent the left and right flank, respectively.

A semi-brittle fractured cantilever tested in [17] is shown in Fig. 6. Subfigure a) depicts the initial crack fabricated by FIB milling, while in Fig. 6 b) the blunted crack before initiating crack growth can be seen. Fig. 6 c) shows the crack evolving from material tearing, bridges, pores and a slight crack path deflection. The results obtained for Δa, δ and α are depicted in the subfigures d), e) and f), respectively. Fig. 6 d) also includes the Δa determined from mechanical data for the respective fracture experiment. The blunting leads to an almost constant crack length and increasing δ and α, shown in Fig. 6 d), e) and f). Additionally, contrast changes through out the experiment can be seen in the *in situ* frames.

The algorithm's generalization was examined by processing *in situ* frames acquired by TEM imaging and performed with a different measurement setup, illustrated in Fig. 7. The initial crack is depicted by subfigure a) and the fully blunted evolved crack is illustrated in subfigure b). In Fig. 7 b), the material at the crack tip starts to tear and a significant contrast change is visible, indicating crack initiation. Fig. 7 c) depicts the crack contour detail of the *in situ* frame shown in Fig. 7 b), highlighting possible blunting regimes in blue and red. The results determined from the acquired *in situ* frames are displaced for Δa, δ and α in subfigures d), e) and f), respectively.

3.2. Algorithm vs. human expert

In addition to the representative samples above, the algorithm was applied to several additional fracture experiments to validate its generalization capabilities and accuracy. Multiple manual measurements were performed on each sample, too. The mean and standard deviation for the manually measured crack tip coordinates (x, y), as well as δ and α, were calculated and the mean was used as ground truth estimate. To assess the manual measurement error, the mean (e_m) and standard deviation (std_m) were determined for each sample, using the variance of the individual frame to get a single value, comparable to the mean squared error, tabulated in Table 2. The standard deviation was calculated to emphasize the variability of manual measurement error. The error of the algorithm (e_a) was evaluated based on the Euclidean distance between the estimated ground truth and the algorithms output, which was obtained for each individual frame. There, $d_{x,y}$ and δ are given in pixels, while α is stated in degrees to enhance comparability, as the experiments were performed at different magnifications. The experiments in the Table 2 are grouped according to the fracture behavior, with samples B1-B3 representing brittle fracture, D1 indicating ductile failure, and all others samples, SB1-SB6, fractured semi-brittle.
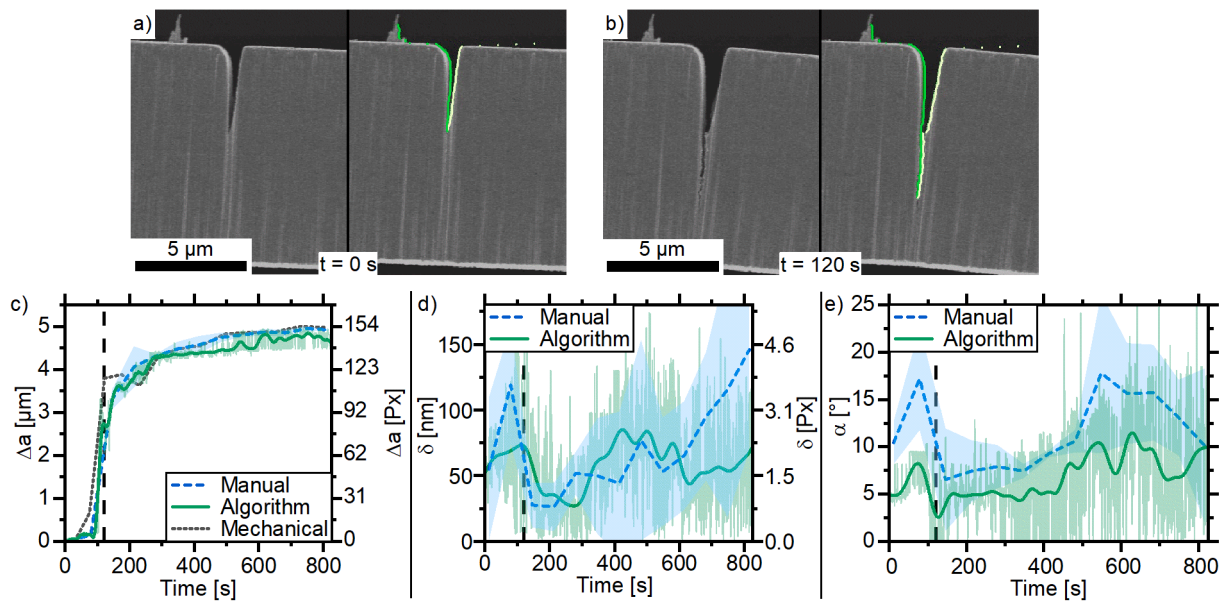
Fig. 5. Fracture characteristics measured for representative unstable fracture. The recorded *in situ* frames are shown in a) and b). The left image illustrates the frame acquired and right image depicts the contour lines found by the algorithm. c) crack extension (Δa), d) crack tip opening displacement (δ) and e) -angle (α). The dashed lines in the graphs represent the *in situ* frames shown in subfigure a) and b). The cantilever was previously tested in [17].
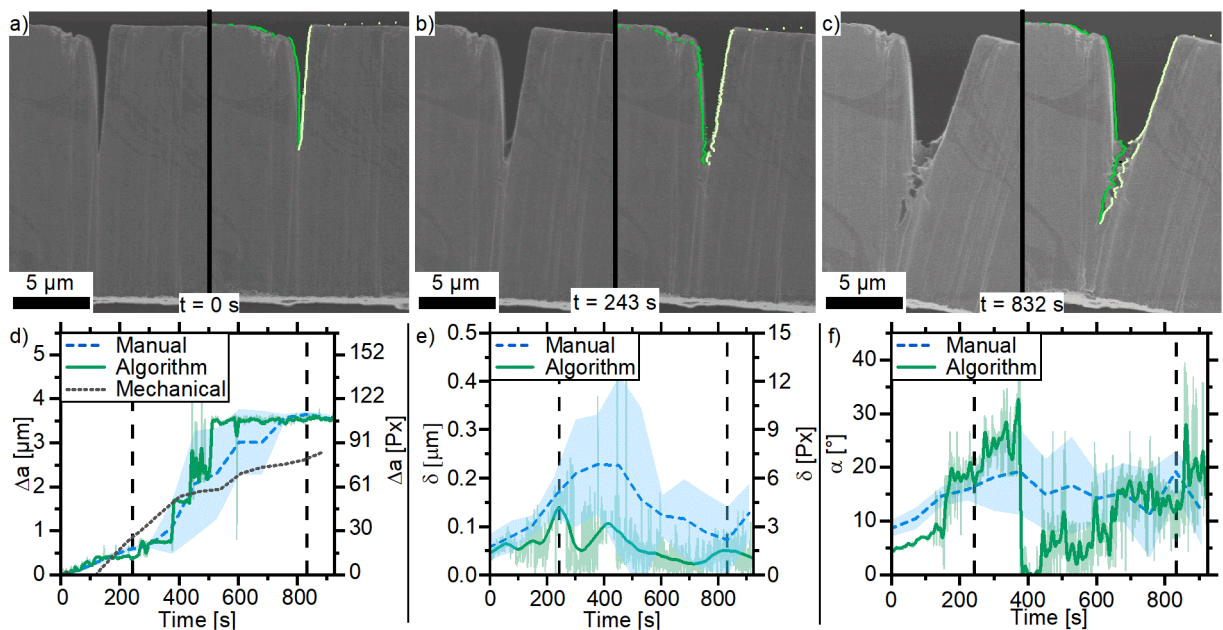

Fig. 6. Comparison of the fracture characteristic measured for a semi-brittle fracture. a)-c) Illustrate the recorded *in situ* frames. The original frame to the left and the processed frame with the determined contours to the right, respectively. The diagrams depict, d) the crack extension (Δa), e) crack tip opening displacement (δ) and f) -angle (α). The *in situ* frames are indicated by the dashed lines. The cantilever was previously tested in [17].

4. Discussion

The evaluation of *in situ* frames enables direct investigation of fracture processes. The algorithm allows for a continuous and automatic evaluation in a short period of time, usually within minutes. Although the image-based evaluation faces various challenges, stemming from the sample mounting, the image formation process and the fracture process itself (Fig. 1). How the algorithm deals with those challenges is discussed in the next section, followed by comparing the performance to human expert measurements and other possible approaches for retrieving data from images. The last section discusses the utilization of the algorithm to determine the local fracture behavior in detail and compares the results to literature data.

4.1. Fracture behavior challenges

Capturing continuous crack propagation necessitates high image acquisition rates, contradicting with high quality imaging in electron microscopy, e.g. a high quality SEM-image requires several seconds of acquisition. Thus, the acquisition rate is usually set to 1 frame/s, representing a good trade-off between following crack propagation and obtaining sufficient image quality. However, the frames retain some amount of noise and the feature resolution is limited by the pixel size. Faint features may perish and go undetected. Furthermore, the *in situ* frames capture only the surface section of the possibly jagged and curved crack front, meaning the crack front shape is a superposition of the local microstructure and stress state [11,20].
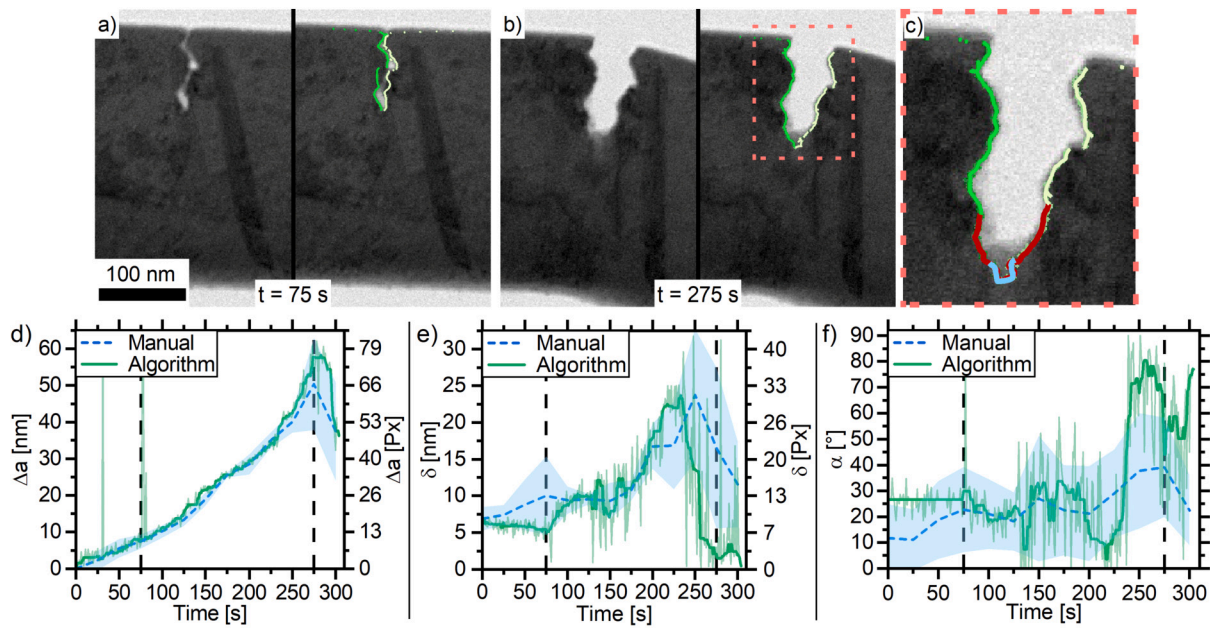
Fig. 7. Fracture characteristics extraction for a sample tested inside a transmission electron microscope. a) and b) show the recorded *in situ* frames. To the left the recorded frame and to the right the processed frame with the crack contour lines found. c) Depicts the crack tip detail of subfigure b), highlighting different possible blunting regions in blue and red. The diagrams depict d) the crack extension (Δ*a*), e) crack tip opening displacement (δ) and f) -angle (α). The dashed lines in the diagrams mark the *in situ* frame.

Table 2

Accuracy assessment of the manual and algorithmic determined crack tip coordinates (x, y), crack tip opening displacement (δ) and -angle (α) for brittle (B1-B3) [17], ductile (D1, Fig. 7) and semi-brittle (SB1-SB6) [10,17] fractured samples. For these values the mean squared error ($\overline{e}$) was evaluated. To assess the crack length error, the Euclidean distance ($d_{x,y}$) of (x, y) to the ground truth data was evaluated. The subscripts a and m refer to algorithmic and manual measured data, respectively. Additionally, for the manual measurement the standard deviations (std_m) was calculated to emphasize the manual measurement variability.

Sample	$d_{x,y}$ [pixel]			$\Delta\delta$ [pixel]			$\Delta\alpha$ [°]		
	$\overline{e}_a$	$\overline{e}_m$	std_m	$\overline{e}_a$	$\overline{e}_m$	std_m	$\overline{e}_a$	$\overline{e}_m$	std_m
B1	8.2	5.0	7.0	0.9	1.7	1.6	4.41	4.72	4.86
B2	22.2	7.4	8.9	1.1	1.1	1.1	6.32	2.44	1.92
B3	15.4	2.8	3.5	1.8	1.9	1.8	5.90	5.03	4.66
D1	3.3	9.4	12.3	5.3	6.7	8.0	13.66	16.86	11.80
SB1	9.6	17.9	22.5	2.6	2.5	1.7	6.95	5.07	2.64
SB2	119.9	6.9	10.0	5.8	2.8	2.8	16.11	2.85	2.79
SB3	10.8	4.8	6.0	2.6	2.9	3.4	6.79	5.67	5.20
SB4	7.8	6.2	7.4	1.3	2.4	2.5	10.77	10.85	11.96
SB5	30.2	38.5	5.9	2.9	3.5	1.7	6.28	9.33	3.50
SB6	17.9	7.9	9.7	5.1	3.0	3.7	7.45	4.94	4.41

While only a narrow crack is evident in Fig. 5 b), the image-based measurements both manual and calculated by the algorithm yielded a similar crack extension throughout the experiment (Fig. 5 c)). However, the crack extension derived from mechanical data produced a higher crack extension of about 200 nm (~6 pixel) directly after fracture. This difference stems from aforementioned limitations of resolving sub-pixel crack separation features. In the case of an ideal straight crack, the crack's feature thickness can be approximated by δ, which does not exceed ~72 nm (2.2 pixels) in this example. By accounting for noise and possible pixel errors, the crack close to the crack tip resembles to be a thin undetected feature. In contrast to the crack extension, δ and α are sensitive to slight changes in the crack shape, due to the crack flank fitting procedure and the uncertainty of crack tip location, which leads to increased scatter. Outside of these understandable, minor deviations, the automatically determined values for δ and α are in good agreement with the manually measured fracture characteristics. Thereby, δ and α exhibit a drop after crack propagation initiation, which is obvious as the blunting regime ends (*t* = 104 s) and brittle failure occurs. Despite the

brittle fracture, the crack stopped and the remaining ligament (~1 μm) fully plasticized, starting at *t* = 300 s. This leads to a constant Δ*a*, while δ and α slightly increase until the end of the experiment, in accordance with the general yielding of the remaining ligament after crack extension, as shown in Fig. 5 d) and e).

In the blunting regime of the semi-brittle sample, the algorithmic results closely match to the manual measurements and are in accordance with the results from mechanical data, outlined in Fig. 6 d)-f), up to *t* = 243 s, where the crack initiates. During crack propagation, additional crack features form, such as pores, material tearing and -bridging, illustrated by the evolved crack in Fig. 6 c). As a result, locating the crack tip and defining the crack contours during crack propagation is challenging. Therefore, the manual measurement displayed increased uncertainty, and the algorithm's results exhibited increased scatter, shown in Fig. 6 d)-f). Nevertheless, for the algorithmic data at crack propagation initiation, a drop in δ and α is evident. During crack propagation, δ is constant and α raises, which is in accordance with the determined crack extension increase at *t* = 243 s, depicted in
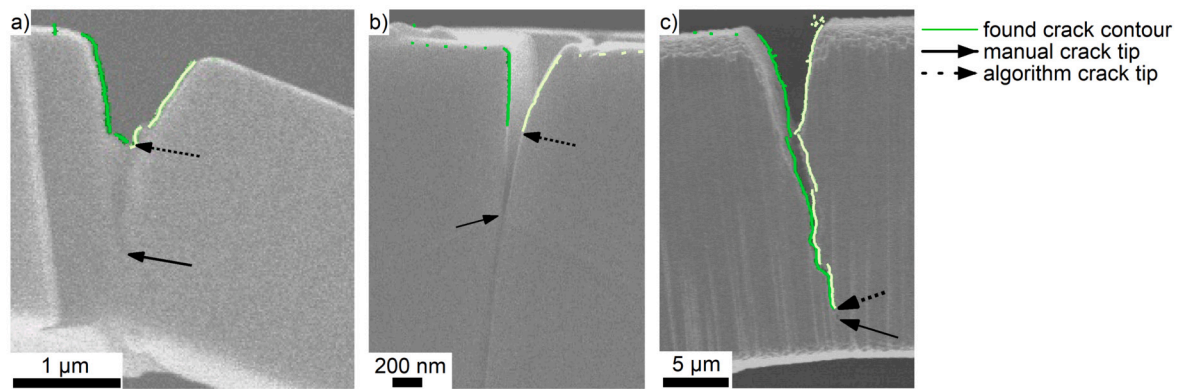
Fig. 8. Respective *in situ* frames for possible detection challenges for automated crack detection. a) SB2 displaying material in the crack wake and contrast changes along the crack flanks, tested in [10]. b) SB6 illustrates a cantilever after semi-brittle fracture exhibiting material in the crack wake and blurred crack flanks, tested in [21]. c) Brittle fractured sample B3 exhibiting a faint crack extension, tested in [17].

Fig. 6 d). Despite the agreement of the data retrieved from the images, the mechanical evaluation resulted in a shorter crack extension of about 800 nm (~24 pixels) for the last unloading step. This difference is possibly due to heterogeneous propagation of the crack front, stemming from semi-brittle fracture and the fact that mechanical evaluation averages over the whole crack front, while the images capture only the surface. In general, the crack length exhibits minor deviations exclusively over the crack front [20].

The sample tested inside the TEM underwent ductile fracture and exhibited extensive blunting, depicted by Fig. 7 a) and b). These frames illustrate the enhanced contrast obtained between background and sample, improving the classification process compared to SEM recordings. Additional features are present inside the sample region, such as dislocation lines, shear bands, crystal orientation, atomic mass and thickness contrast, depicted by the *in situ* frames in Fig. 7. These features originate in the TEM imaging process [38] and complicate crack tip localization. Teared material is visible in Fig. 7 b) in the light gray region at the crack tip, which slightly blurs the surrounding material. Material tearing raised the manual measurement uncertainty for Δa and δ significantly, noted by blue shaded region in Fig. 7 d) and e). This occurred due to the absence of sharp crack edges and made crack localization near the crack tip more challenging. The angle α seems unaffected by material tearing, but exhibits significant scatter throughout the experiment, masking any potential effect of material tearing. The scatter in α can be attributed to the curved shape of the crack, which complicates the crack flank fitting procedure. The algorithm encounters the same visual obstacles as the manual measurement. Prior to the material tearing regime, the algorithmically determined and manually measured data is in accordance (Fig. 7 e)-f)). Up to $t = 225$ s, Δa and δ increase monotonically, while α remains constant, indicating crack blunting. After this frame, material tearing occurs and the algorithm defines the teared material, shown by the light gray area in Fig. 7 b), as cracked. As a result, the algorithm determined a slightly enhanced crack growth with decreasing δ, while α increased due to the blurred transition from blunted crack to crack flank. Several manual measurements revealed that the teared material is neglected as often as it is included in the crack shape measurements. This resulted in an increased uncertainty of the manual measurement after $t = 225$ s. At unloading, crack closure occurs due to the elastically stored energy, which induces a drop in Δa and δ.

The different fracture behaviors brittle, ductile and semi-brittle revealed a variety of topological crack features, which complicate crack detection. The features can be split into classification and evaluation related issues. For example, faint crack associated with brittle fracture makes it challenging to detect the crack completely and is related to the classification process. Contrarily, crack tip blunting in ductile fracture blurs the transition between blunt crack tip and the flanks. While this complicates the evaluation process, it simplifies classification due to an increased feature size. Material tearing and -bridging in ductile fracture increases the challenge of classifying the crack due to material left in the crack wake. Semi-brittle fracture can cause void formation, crack deflection and bifurcation, which makes distinct crack classification even more challenging. Due to these features, the crack flanks tend to be jagged and curved, complicating the fracture characteristic evaluation. In addition to these features, the cantilever alignment, with respect to the viewing direction, affects fracture characteristic evaluation, as the SEM views only a 2D plane of the 3D cantilever. Thus, cantilever misalignments, *e.g.* slight rotation around y-axis, see Fig. 1 a), result in visible side surfaces, complicating crack contour detection.

4.2. Algorithm vs. human expert

Manual measurements are frequently used to evaluate *in situ* images obtained from fracture experiments. Thus, the results determined by the algorithm were compared to manual measurements to assess the algorithms accuracy and its capability to localize the crack tip as well as extract δ and α. The results for the different fracture characteristics are listed in Table 2. Thereby, the overall error of the manual measurement illustrates the challenge of extracting fracture characteristics. In general, errors obtained by manual and algorithmic measurements are of the same order of magnitude, although, the algorithmic errors are slightly higher. For the semi-brittle fractures, SB2 and SB6, the algorithmic errors are higher by multiple orders of magnitude. For these samples, the algorithm failed to completely detect the crack flanks, due to background material visible from the onset of the measurement, noted by Fig. 8 a) and b). Manual crack detection benefits from human extrapolation capabilities of the crack flanks, which leads to smaller variations. However, the crack flanks are blurred in SB6, depicted by Fig. 8 b), which impairs human perception and increases the manual measurement error and variability.

In the case of brittle fracture, the increased $d_{x,y}$ errors of the algorithm can be attributed to the thinness of the crack, see the thin crack extension in Fig. 5 b) and Fig. 8 c). The algorithmic errors of δ and α are in accordance with the manual measurement errors and within in the error variability of the manual measurement, despite the undetected portion of the crack. δ and α seem unaffected by the excluded faint crack due to a smaller crack opening, demonstrating the applicability of the algorithm for brittle failure.

The ductile fractured sample D1 evidenced a similar scatter of $d_{x,y}$ for the manual measurement, while δ and α exhibited an increased scatter, possibly stemming from crack tip blunting. Besides, crack tip blunting caused raised absolute values of δ. Thus, the increased scatter has a negligible affect on the δ measurement. Comparing the algorithm to the manual measurement, all errors are below the manual measurement errors, which can mainly be attributed to the enhanced

image contrast and crack tip blunting, all of which benefit the classification process. This is supported by the measurement curves depicted in Fig. 7 d)-f). Despite small deviations, the algorithm performs well for samples undergoing ductile fracture. Even though only a single ductile fractured sample was analyzed the repeating sequence of blunting, tearing and pore formation is characteristic of ductile failure, proofing the algorithm's capabilities.

Semi-brittle fracture complicates fracture characteristic evaluation due to the combination of features from brittle and ductile fracture, as well as the aforementioned additional fracture features. Thus, the manual measurement error exhibits an increased scatter for all fracture characteristics, compared to the brittle samples, due to additional features and the higher absolute values of δ and α. Despite the additional features, the error of the semi-brittle samples is reduced compared to the fully ductile sample, which may stem from the reduced absolute values of the individual characteristics and the differences in imaging conditions between SEM and TEM. The algorithmically determined fracture characteristics exhibited an increased error for $d_{x,y}$ and α, as a result of material in the crack wake and the curved crack flanks. However, the majority of the algorithmic errors are of the same order of magnitude as the manual measurement errors, pointing to the capabilities of the algorithm in analyzing semi-brittle failure. The algorithm successfully accounts for the additional complications, illustrated by Fig. 1 d), that appear during semi-brittle fracture.

Besides the comparison of the resulting fracture characteristics, time constrains are an uprising issue. In general, manual measurements are time consuming, so only critical frames are evaluated, leading to sparse information about the fracture process. Manual measurement also includes a lot of scatter due to human individuality. The algorithm, on the other hand, allows all *in situ* images to be analyzed within minutes and offers increased data density. Furthermore, the automatic procedure results in an independent evaluation, benefiting the reproducibility of the data.

4.3. Comparison to other techniques and possible enhancements

To evaluate *in situ* frames acquired from mechanical experiments, digital image correlation (DIC) is frequently conducted [5,39–47]. DIC tracks sample changes by correlating image-subsets of consecutive images [39,40]. The tracked sample changes can then be translated into sample deformations, allowing local strains to be determined [39,40,43–50]. These local strains are used to detect cracks and estimate the stress intensity factor [41,51,52]. The application to consecutive images facilitates tracking of crack propagation [42,53,54]. For macroscopic experiments Chen et al. [55] additionally determined δ and α by DIC. They achieved this by applying a wavelet transform to the displacement fields, enabling crack shape extraction. The δ was evaluated by using the crack shape as mask over the displacement field in x-direction, giving the crack flank displacement for each pixel. To obtain α the crack shape was quadratically fitted and the angle was measured at fixed distances from the crack tip. DIC is an advanced method, relying on the recognition of self-similar surfaces structures between consecutive images [5,39,40,48,50]. Thus, the sample surfaces are patterned to enhance surface structure recognition and suppress image noise [5,48]. To enable a high resolution imaging of the strain field, acquisition rates below 1 frame/minute are necessary [5,43,46,47]. This is unfeasible for the continuous crack growth monitoring during fracture experiments [5]. To enhance the image acquisition rate, Alfreider et al. [56] used a coarse grid pattern on the sample surface, at the cost of a lower strain field resolution. Due to the lower resolution, the crack shape can not be accurately determined from the *in situ* frames, leading to an imperfect crack shape. Furthermore, samples tested inside a TEM exhibit changing image contrast in the sample region due to the imaging conditions. This renders classical DIC between frames infeasible. The presented algorithm in this work requires no self-similar structures on the sample surface and is capable of detecting the crack

shape on an individual pixel basis, causing a flexible application to different testing setups inside SEMs and TEMs. Furthermore, the similar performance of the algorithm and manual measurements proved the applicability of the algorithm to different fracture behaviors. This allows the fracture characteristics (Δa, δ and α) to be automatically extracted from noisy *in situ* frames.

Nevertheless, the capabilities of the algorithm would benefit from an enhanced classification process. This could be achieved by using a more sophisticated classifier, such as convolutional neural networks, *e.g.* U-net [57,58] or Segment Anything [59,60]. Although these classifiers might improve the overall performance of the algorithm, they require a lot of annotated input data for training, testing and validation. Another enhancement to the algorithm would be to include the time series information from subsequent images in the classification and evaluation process. This would make it possible to know the crack path before the classification and extraction of the crack contour, which would decrease the scatter of fracture characteristic data. Additionally, the crack flank fitting could be initialized by previously determined parameters. Besides, increasing the input image quality, through increased image resolution, contrast enhancement and decreased image noise would improve any image-based evaluation process. Lenthe et al. [61] found that during SEM imaging at high image acquisition rates, a pixel shift can occur due to the scanning process, resulting in image noise and blurred edges. To avoid this, they applied a correction function during the image formation process, leading to a decrease in pixel noise and sharper features.

4.4. Fracture mechanical implications

The fracture characteristics determined from *in situ* images allow a direct evaluation of the fracture process, based on the correlation of δ and α to the J-integral [8,62]. Additionally, recording the crack length enables the calculation of the J-integral without the necessity of quasi-static or dynamic loading to determine the cantilever stiffness throughout the experiment. However, the initial cantilever stiffness is required to convert the crack lengths measured by the algorithm into stiffness [10]. The initial cantilever stiffness can be obtained from a static pre-loading in the elastic regime or numerically estimated by Euler-Bernoulli beam theory [10]. This means that the fracture characteristics δ and α determined continuously by the algorithm allows the construction of crack-growth resistance curves (R-curves) without further parameter calculation. Compared to manual measurements and quasi-static loading, the automatic evaluation by the algorithm gives a higher data point density [5,11], making the transition from blunting to crack growth more obvious. For the representative samples in Fig. 5, Fig. 6 and Fig. 7, the resultant R-curves are depicted in Fig. 9 a), b) and c), respectively. In the blunting regime, all R-curves are increasing. The end of the blunting regime is indicated by the dotted vertical line in Fig. 9. This increase matches the typical R-curve behavior described in the ASTM1820 standard [9]. After crack initiation, the R-curve behavior starts to deviate. The brittle fractured sample (B1) exhibits a slight rise in δ and a decrease in α after crack initiation up to a crack extension of 2.5 μm, see Fig. 9 a). Following the ASTM1820 standard, the maximum crack extension capacity (Δa_{max}) is 1/4 of the initial ligament length ($\Delta a_{max} = 0.25(W - a_0)$) [9,63], indicated by the gray shaded regions in Fig. 9. In the case of sample B1, Δa_{max} is reached at a crack extension of 1.5 μm. This leads to the typical R-curve shape from $\Delta a = 0$ μm to $\Delta a_{max} = 1.5$ μm [9,63]. However, above Δa_{max} the R-curves of δ and α continue with the same trend until the remaining ligament fully plastifies at $\Delta a \approx 3$ μm. At this point, crack propagation is slowed due to reduced energy storing capabilities stemming from geometrical constrains, leading to purely plastic deformation. In conjunction, the manual measurements resulted in a similar R-curve as the algorithmic measurements. However, an increased scatter is observed for the manual measurements, which originates from a low number of measurement points.
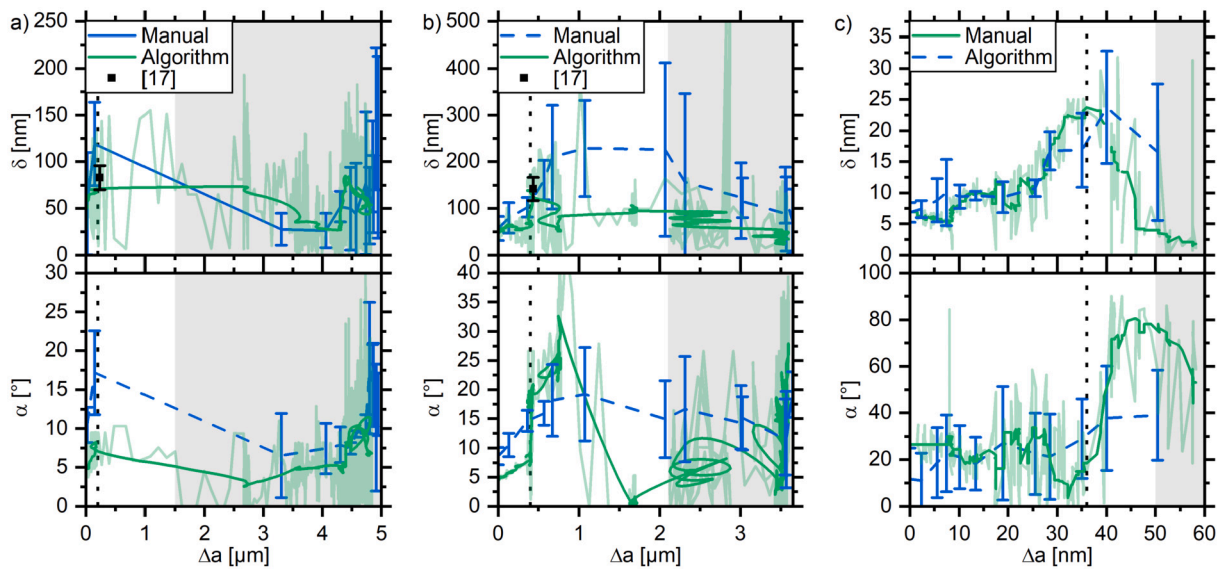
Fig. 9. R-curves obtained for the crack tip opening displacement (δ) and -angle (α) for the representative samples B1, SB1 and D1, illustrated by the subfigures a), b) and c), respectively. The black data point in a) and b) was measured in [17].

In case of the semi-brittle (SB) sample, δ decreases immediately at crack initiation, while α still increases. At the crack initiation ($\Delta a = 0.4$ μm) the crack sharpens, leading to an increase in α and Δa, while δ decreases, see Fig. 9 b) and Fig. 6 b). Also, at this time, pores form in front of the crack. The material bridges, between crack and pore, fracture later to connect them, leading to a decrease in α and enhanced crack growth rate at $\Delta a = 0.7$ μm, illustrated in Fig. 9 b). The fractured material bridges are observable in Fig. 6 c). Pore formation followed by crack advancement through material bridge failure continuous until the experiments end. This advancement of the crack leads to more challenging crack detection, as described in subsection 4.1, and, as a result, scatter increases. The manual measurements also exhibited an increased scatter, especially after crack initiation, leading to a rising R-curve until $\Delta a = 2$ μm. The algorithmically determined R-curve mostly resides within the increased scatter of the manual measurement.

The ductile sample (D1) exhibits a similar R-curve behavior to SB1. The crack sharpening after crack initiation is depicted by the *in situ* frames in Fig. 7 b) and c). At $\Delta a \approx 50$ nm, α starts to decrease and the reduction of δ is damped, indicating continuous crack growth. Compared to the SB1 sample, no pore formation was observed, pointing to stable crack growth.

The correlation between *in situ* frames and the measured fracture characteristics by the algorithm can be best illustrated by a video. In the supplementary material, videos can be found for the representative samples discussed in this section. These illustrate the measurement of δ and α correlated to the *in situ* frames, for brittle (B1, Supplementary video A), semi-brittle (SB1, Supplementary video B) and ductile (D1, Supplementary video C) fracture.

Nevertheless, the decrease of δ after crack initiation and latter the α drop contradicts the typical R-curve [9,63]. This deviation occurs as the algorithm measures δ and α locally at the crack tip, while the ASTM1820 standard defines δ and α at the initial crack position [9], depicted by the red and green measurement marks in Fig. 10, respectively. Therefore, the standard assumes homogeneous stress and strain fields, as well as isotropic material deformation throughout the fracture experiment [9,63]. Nevertheless up to crack initiation, the local measurement equals the measurement defined in the standard, noted the blunted crack to the left in Fig. 10. The J-integral evaluation from mechanical data has similar constrains, as it expects a homogeneous stress and strain field [9,63]. To compare the obtained values with literature, only the crack initiation point is considered, which was determined by visual inspection of the *in situ* frames. For the B1, SB1
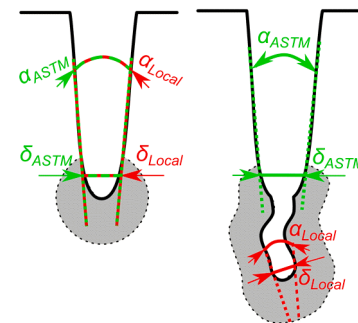

Fig. 10. Different approaches to measure crack tip opening displacement (δ) and -angle (α) during crack tip blunting and crack growth. Green illustrates the measurement defined by the ASTM1820 standard. Red depicts the local measurement performed by the algorithm. The gray shaded region represents the plasticized region around the crack.

and D1 samples, the crack initiation occurred at $t = 97$ s, 248 s and 233 s, respectively. The δ results determined by the algorithm at the initiation points are translated into fracture toughness values utilizing Equation (3) and Equation (4). The results are summarized in Table 3.

The values determined for δ by the algorithm are in good agreement with manual measurement values from literature. Furthermore, the measurement errors are on the same order of magnitude, indicating a similar accuracy between the algorithm and manual measurements, outlined in Table 3. Moreover, conversion to the J-integral (J_q) and stress intensity (K_q) allows a direct comparison to the mechanically determined fracture characteristics reported in literature. The values obtained for J_q and K_q by the algorithm are in accordance with the mechanical literature data, though the errors of the algorithm are slightly increased. Nevertheless, the similarity of the respective fracture characteristics supports the potential of the algorithm to evaluate fracture experiments in the field of micromechanics. The algorithm is independent of the material properties and relies only on the 2D representation of the crack. Hence, as long as the material is reasonably isotropic, the crack on the surface would be related to the crack front inside the specimen and the evaluation is valid. Notably, elastic plastic fracture mechanics is based on the same assumption and assumes an isotropic homogeneous material [5,20,63]. Thus, the algorithm necessitates similar material properties as commonly employed in fracture mechanics. Furthermore, the R-curves obtained from the *in situ* frames allow to deepen the knowl-

Table 3

Crack tip opening displacement δ determined by the algorithm at the crack initiation point for the exemplary shown cantilevers in Fig. 5, Fig. 6 and Fig. 7. The δ values for B1 and SB1 are compared to manual measurements values found in literature [17], denoted by the subscript m. Additionally, for comparison with mechanical data, δ was transformed into the J-integral J_q and stress-intensity K_q according to Equation (3) and Equation (4).

sample	δ_a [nm]	$J_{\delta_a,q}$ [$\frac{J}{m^2}$]	$K_{\delta_a,q}$ [MPa $\sqrt{m}$]	δ_m [nm]	$J_{\delta_m,q}$ [$\frac{J}{m^2}$]	$K_{\delta_m,q}$ [MPa $\sqrt{m}$]	J_q [$\frac{J}{m^2}$]	K_q [MPa $\sqrt{m}$]
B1	72 ± 24	190 ± 64	6.8 ± 2.3	83 ± 14	219 ± 37	7.3 ± 0.6	180 ± 6	6.7 ± 0.1
SB1	135 ± 15	390 ± 43	9.8 ± 1.1	142 ± 25	400 ± 71	9.9 ± 0.9	398 ± 14	9.9 ± 0.2
D1	23 ± 5	37 ± 7	2.7 ± 0.5	21 ± 3	34 ± 5	2.6 ± 0.4	41 ± 3	2.8 ± 0.2

edge of the fracture process occurring at the micron and sub-micron scale. Thus, the presented evaluation can be used in conjunction with mechanical calculations to characterize the fracture process and verify the validity of small-scale experiments [11,17,21]. Additionally, the fracture characteristics can directly be related to the micro structure using the available crack path information. This provides further insight into fracture processes with unexpected or unknown material behavior due to inhomogeneities or local microstructural variations [64–66]. By extending the algorithms capabilities to account for multiple fracture paths, even more complex fracture processes could be investigated.

5. Conclusion

An algorithm was developed that automatically adapts to the image input data of *in situ* experiments to provide deeper insight into the fracture process at the micron to sub-micron scale. This algorithm extracts the crack length and additional fracture characteristics such as crack tip opening displacement (δ) and -angle (α). The extraction process was split into a probabilistic classification, contour extraction, and evaluation of the fracture characteristics from the identified crack contours. For the development of the algorithm, samples exhibiting brittle, semi-brittle and ductile failure were used to cover the full range of fracture behavior and corresponding fracture features. For comparison, the crack length was also determined from mechanical stiffness data and manual measurements to access the accuracy of the image-based measurement. This comparison revealed an overall excellent agreement between the image and mechanical-based measurements. Several frames of each sample were manually evaluated multiple times to serve as ground truth data for the crack tip coordinates, crack tip opening displacement and -angle. This ground truth data was used to verify the performance of the algorithm, indicating comparable accuracy to manual measurements and proving the applicability of the algorithm on different fracture behaviors. This novel algorithm reproducibly evaluates all recorded *in situ* frames in minutes, compared to time intense manual process, requiring highly skilled experts. Analysis of crack tip opening displacement and -angle allows the verification of fracture toughness values calculated from mechanical data. The image-based evaluation allows fracture processes of more complex material structures to be evaluated, including materials with anisotropic properties and increased blunting tendency. In summary, this novel algorithm provides a powerful tool aid the understanding of complicated fracture processes and allows a more detailed understanding of the fundamental fracture processes of complex material structures at the micro- and nano scale.

CRediT authorship contribution statement

K. Schmuck: Writing – review & editing, Writing – original draft, Methodology, Data curation, Conceptualization. **M. Antenreiter:** Writing – review & editing, Writing – original draft, Methodology, Data curation, Conceptualization. **M. Alfreider:** Writing – review & editing, Methodology. **D. Kiener:** Writing – review & editing, Supervision, Resources, Project administration, Funding acquisition, Conceptualization.

Declaration of competing interest

The authors declare that they have no known competing financial interests or personal relationships that could have appeared to influence the work reported in this paper.

Data availability

Data will be made available on request.

Appendix A. Supplementary material

Supplementary material related to this article can be found online at https://doi.org/10.1016/j.matdes.2024.113038.

References

[1] G. Dehm, B.N. Jaya, R. Raghavan, C. Kirchlechner, Overview on micro- and nanomechanical testing: new insights in interface plasticity and fracture at small length scales, Acta Mater. 142 (2018) 248–282, https://doi.org/10.1016/j.actamat.2017.06.019.

[2] D.S. Gianola, A. Sedlmayr, R. Mnig, C.A. Volkert, R.C. Major, E. Cyrankowski, et al., In situ nanomechanical testing in focused ion beam and scanning electron microscopes, Rev. Sci. Instrum. 82 (6) (2011) 1–12.

[3] P. Hosemann, Small-scale mechanical testing on nuclear materials: bridging the experimental length-scale gap, Scr. Mater. 143 (2018) 161–168, https://doi.org/10.1016/j.scriptamat.2017.04.026.

[4] G. Sernicola, T. Giovannini, P. Patel, J.R. Kermode, D.S. Balint, T.B. Britton, et al., In situ stable crack growth at the micron scale, Nat. Commun. 8 (1) (2017), https://doi.org/10.1038/s41467-017-00139-w.

[5] D. Kiener, M. Wurmshuber, M. Alfreider, G.J.K. Schaffar, V. Maier-Kiener, Recent advances in nanomechanical and in situ testing techniques: towards extreme conditions, Curr. Opin. Solid State Mater. Sci. 27 (6) (2023) 101108, https://doi.org/10.1016/j.cossms.2023.101108.

[6] J. Ast, B. Merle, K. Durst, M. Göken, Fracture toughness evaluation of NiAl single crystals by microcantilevers - a new continuous J-integral method, J. Mater. Res. 31 (23) (2016) 3786–3794.

[7] J. Ast, M. Ghidelli, K. Durst, M. Göken, M. Sebastiani, A.M. Korsunsky, A review of experimental approaches to fracture toughness evaluation at the micro-scale, Mater. Des. 173 (2019) 107762, https://doi.org/10.1016/j.matdes.2019.107762.

[8] S. Wurster, C. Motz, R. Pippan, Characterization of the fracture toughness of micro-sized tungsten single crystal notched specimens, Philos. Mag. 92 (14) (2012) 1803–1825.

[9] ASTM Standard, Standard Test Method for Measurement of Fracture Toughness, ASTM Book of Standards, 03.01 (January) 2013, pp. 1–54.

[10] M. Alfreider, D. Kozic, O. Kolednik, D. Kiener, In-situ elastic-plastic fracture mechanics on the microscale by means of continuous dynamical testing, Mater. Des. 148 (2018) 177–187, https://doi.org/10.1016/j.matdes.2018.03.051.

[11] K.S. Schmuck, M. Alfreider, D. Kiener, Crack length estimations for small - scale fracture experiments via image processing techniques, J. Mater. Res. 37 (17) (2022) 2848–2861, https://doi.org/10.1557/s43578-022-00681-4.

[12] C.F. Shih, Relationship between the J-integral and the COD for stationary and extending cracks, J. Mech. Phys. Solids 29 (4) (1981) 305–326.

[13] J. Heerens, M. Schödel, Characterization of stable crack extension in aluminium sheet material using the crack tip opening angle determined optically and by the δ5 clip gauge technique, Eng. Fract. Mech. 76 (1) (2009) 101–113, https://doi.org/10.1016/j.engfracmech.2008.04.009.

[14] U. Zerbst, M. Heinimann, C.D. Donne, D. Steglich, Fracture and damage mechanics modelling of thin-walled structures - an overview, Eng. Fract. Mech. 76 (1) (2009) 5–43, https://doi.org/10.1016/j.engfracmech.2007.10.005.

[15] British Standards Institution, Methods for Crack Opening Displacements (COD) Testing, DD 19:1972, 1972, p. 48.

[16] M. Wurmshuber, M. Alfreider, S. Wurster, R. Pippan, D. Kiener, Small-scale fracture mechanical investigations on grain boundary doped ultrafine-grained tungsten, Acta Mater. 250 (118878) (2023) 18, https://doi.org/10.1016/j.actamat.2023.118878.

[17] K. Schmuck, M. Burtscher, M. Alfreider, M. Wurmshuber, D. Kiener, Micromechanical fracture investigations on grain size tailored tungsten-copper nanocomposites, JOM (2024), https://doi.org/10.1007/s11837-023-06348-7.

[18] R. Pippan, S. Wurster, D. Kiener, Fracture mechanics of micro samples: fundamental considerations, Mater. Des. 159 (2018) 252–267, https://doi.org/10.1016/j.matdes.2018.09.004.

[19] B.N. Jaya, J.M. Wheeler, J. Wehrs, J.P. Best, R. Soler, J. Michler, et al., Microscale fracture behavior of single crystal silicon beams at elevated temperatures, Nano Lett. 16 (12) (2016) 7597–7603.

[20] A.K. Saxena, S. Brinckmann, B. Völker, G. Dehm, C. Kirchlechner, Experimental conditions affecting the measured fracture toughness at the microscale: notch geometry and crack extension measurement, Mater. Des. 191 (2020) 1–11.

[21] M. Burtscher, M. Alfreider, K. Schmuck, H. Clemens, S. Mayer, D. Kiener, In situ fracture observations of distinct interface types within a fully lamellar intermetallic TiAl alloy, J. Mater. Res. 36 (2021) 2465–2478.

[22] G. Van Rossum, F.L. Drake, Python 3 Reference Manual, CreateSpace, Scotts Valley, CA, 2009, Available from: https://www.python.org/.

[23] G. Bradski, The OpenCV library, Dr. Dobb's J. Softw. Tools (2000).

[24] S. van der Walt, J.L. Schönberger, J. Nunez-Iglesias, F. Boulogne, J.D. Warner, N. Yager, et al., scikit-image: image processing in Python, PeerJ (2014).

[25] C.R. Harris, K.J. Millman, S.J. van der Walt, R. Gommers, P. Virtanen, D. Cournapeau, et al., Array programming with {NumPy}, Nature 585 (2020) 357–362.

[26] P. Virtanen, R. Gommers, T.E. Oliphant, M. Haberland, T. Reddy, D. Cournapeau, et al., SciPy 1.0: fundamental algorithms for scientific computing in python, Nat. Methods 17 (2020) 261–272, Available from: https://rdcu.be/b08Wh.

[27] M. Guizar-sicairos, S.T. Thurman, J.R. Fienup, Efficient subpixel image registration algorithms manuel, Opt. Lett. 33 (2) (2008) 156–158.

[28] R.O. Duda, P.E. Hart, Pattern Classification and Scene Analysis, Wiley & Sons, New York, 1973.

[29] T. Pavlidis, Contour filling in raster graphics, Comput. Graph. 15 (3) (1981) 29–36.

[30] J.F. Hughes, A. Van Dam, M. McGuire, D.F. Sklar, J.D. Foley, S.K. Feiner, et al., Computer Graphics Principles and Practice, third edit ed., Addison-Wesley, Upper Saddle River, NJ, 2014.

[31] M.L. Fredman, R.E. Tarjan, Fibonacci heaps and their uses in improved network optimization algorithms, in: 25th Annual Symposium on Foundations of Computer Science, 1984, Institute of Electrical and Electronics Engineers, 1984, pp. 338–346.

[32] R.O. Ritchie, Mechanism of fatigue-crack propagation in ductile and brittle materials, Int. J. Fract. 100 (1998) 55–83.

[33] M.A. Fischler, R.C. Bolles, Paradigm for model, Commun. ACM 24 (6) (1981) 381–395.

[34] R. Hartley, A. Zisserman, Multiple View Geometry, Cambridge University Press, 2004.

[35] J.R. Rice, G.F. Rosengren, Plane strain deformation near a crack tip in a power-law hardening material, J. Mech. Phys. Solids 16 (1) (1968) 1–12.

[36] J.W. Hutchinson, Singular behaviour at the end of a tensile crack in a hardening material, J. Mech. Phys. Solids 16 (1968) 13–31.

[37] M. Burtscher, T. Klein, J. Lindemann, O. Lehmann, H. Fellmann, V. Güther, et al., An advanced tial alloy for high-performance racing applications, Materials 13 (21) (2020) 1–14.

[38] C.B. Carter, D.B. Williams, Transmission Electron Microscopy: Diffraction, Imaging, and Spectrometry, Springer, 2016.

[39] M. Sutton, W. Wolters, W. Peters, W. Ranson, S. McNeill, Determination of displacements using an improved digital correlation method, Image Vis. Comput. 1 (3) (1983) 133–139.

[40] S.R. McNeill, W.H. Peters, M.A. Sutton, Estimation of stress intensity factor by digital image correlation, Eng. Fract. Mech. 28 (1) (1987 jan) 101–112, Available from: https://linkinghub.elsevier.com/retrieve/pii/001379448790124X.

[41] S. Roux, J. Réthoré, F. Hild, Digital image correlation and fracture: an advanced technique for estimating stress intensity factors of 2D and 3D cracks, J. Phys. D, Appl. Phys. 42 (21) (2009).

[42] T. Thäsler, J. Holtmannspötter, H.J. Gudladt, Monitoring the fatigue crack growth behavior of composite joints using in situ 2D-digital image correlation, J. Adhes. 95 (5–7) (2019) 595–613, https://doi.org/10.1080/00218464.2018.1562923.

[43] A.D. Kammers, S. Daly, Digital image correlation under scanning electron microscopy: methodology and validation, Exp. Mech. 53 (9) (2013) 1743–1761.

[44] F. Di Gioacchino, J. Quinta da Fonseca, Plastic strain mapping with sub-micron resolution using digital image correlation, Exp. Mech. 53 (5) (2013) 743–754.

[45] F. Di Gioacchino, W.J. Clegg, Mapping deformation in small-scale testing, Acta Mater. 78 (2014) 103–113, https://doi.org/10.1016/j.actamat.2014.06.033.

[46] T.E.J. Edwards, F. Di Gioacchino, R. Muñoz-Moreno, W.J. Clegg, Deformation of lamellar TiAl alloys by longitudinal twinning, Scr. Mater. 118 (2016) 46–50, https://doi.org/10.1016/j.scriptamat.2016.03.004.

[47] T.E.J. Edwards, X. Maeder, J. Ast, L. Berger, J. Michler, Mapping pure plastic strains against locally applied stress: revealing toughening plasticity, Sci. Adv. 8 (30) (2022) 1–11.

[48] M. Sutton, J.J. Orteu, H. Schreier, Image Correlation for Shape, Motion and Deformation Measurements, Springer, Berlin Heidelberg, 2009.

[49] J. Réthoré, S. Roux, F. Hild, An extended and integrated digital image correlation technique applied to the analysis of fractured samples: the equilibrium gap method as a mechanical filter, Eur. J. Comput. Mech. 18 (3–4) (2009) 285–306.

[50] K. Unterweger, O. Kolednik, The local deformation behaviour of MMCs -an experimental study, Z. Met.kd. (Materials Research and Advanced Techniques) 96 (9) (2005) 1063–1068.

[51] J. Réthoré, F. Hild, S. Roux, Extended digital image correlation with crack shape optimization, Int. J. Numer. Methods Eng. 73 (2) (2008) 248–272.

[52] M. Vidal, M. Ostra, N. Imaz, E. García-Lecina, C. Ubide, Analysis of SEM digital images to quantify crack network pattern area in chromium electrodeposits, Surf. Coat. Technol. 285 (2016) 289–297, https://doi.org/10.1016/j.surfcoat.2015.11.049.

[53] F. Mathieu, F.F. Hild, S. Roux, Identification of a crack propagation law by digital image correlation, Int. J. Fatigue 36 (1) (2012) 146–154, https://doi.org/10.1016/j.ijfatigue.2011.08.004.

[54] T. Strohmann, D. Starostin-Penner, E. Breitbarth, G. Requena, Automatic detection of fatigue crack paths using digital image correlation and convolutional neural networks, Fatigue Fract. Eng. Mater. Struct. 44 (5) (2021) 1336–1348.

[55] H. Chen, J. Shen, D. Scotson, X. Jin, H. Wu, T.J. Marrow, Fracture toughness evaluation of a nuclear graphite with non-linear elastic properties by 3D imaging and inverse finite element analysis, Eng. Fract. Mech. 293 ((October) 2023) 109719, https://doi.org/10.1016/j.engfracmech.2023.109719.

[56] M. Alfreider, M. Meindlhumer, V. Maier-Kiener, A. Hohenwarter, D. Kiener, Extracting information from noisy data: strain mapping during dynamic in situ SEM experiments, J. Mater. Res. 36 (11) (2021) 2291–2304, https://doi.org/10.1557/s43578-020-00041-0.

[57] R. Olaf, F. Philipp, B. Thomas, U-Net: convolutional networks for biomedical image segmentation, in: Medical Image Computing and Computer-Assisted Intervention – MICCAI 2015 MICCAI 2015, in: Lecture Notes in Computer Science, vol. 9351, 2015, pp. 234–241.

[58] N. Siddique, S. Paheding, C.P. Elkin, V. Devabhaktuni, U-net and its variants for medical image segmentation: a review of theory and applications, IEEE Access 9 (2021) 82031–82057.

[59] A. Kirillov, E. Mintun, N. Ravi, H. Mao, C. Rolland, L. Gustafson, et al., Segment anything, Computer Vision and Pattern Recognition, Available from: http://arxiv.org/abs/2304.02643, 2023.

[60] J.F. Keckes, A. Jelinek, D. Kiener, M. Alfreider, Neural network supported microscale in situ deformation tracking: a comparative study of testing geometries, JOM (2024), https://doi.org/10.1007/s11837-024-06437-1.

[61] W.C. Lenthe, J.C. Stinville, M.P. Echlin, Z. Chen, S. Daly, T.M. Pollock, Advanced detector signal acquisition and electron beam scanning for high resolution SEM imaging, Ultramicroscopy 195 (2018) 93–100, https://doi.org/10.1016/j.ultramic.2018.08.025.

[62] R.O. Ritchie, The conflicts between strength and toughness, Nat. Mater. 10 (11) (2011) 817–822, https://doi.org/10.1038/nmat3115.

[63] T.L. Anderson, Fracture Mechanics, 3rd ed., CRC Press, 2005.

[64] B.L. Boyce, S.L.B. Kramer, H.E. Fang, T.E. Cordova, M.K. Neilsen, K. Dion, et al., The sandia fracture challenge: blind round Robin predictions of ductile tearing, Int. J. Fract. 186 (1–2) (2014) 5–68.

[65] B.L. Boyce, S.L.B. Kramer, T.R. Bosiljevac, E. Corona, J.A. Moore, K. Elkhodary, et al., The second Sandia Fracture Challenge: predictions of ductile failure under quasi-static and moderate-rate dynamic loading, Int. J. Fract. 198 (1–2) (2016) 5–100.

[66] S.L.B. Kramer, A. Jones, A. Mostafa, B. Ravaji, T. Tancogne-Dejean, C.C. Roth, et al., The Third Sandia Fracture Challenge: Predictions of Ductile Fracture in Additively Manufactured Metal, vol. 218, Springer, Netherlands, 2019.